Title

Impact of n-Butylammonium Bromide on the Chemical and Electronic Structure of Double-Cation Perovskite Thin Films

Journal

ACS Applied Materials & Interfaces, 13(44)

ISSN

1944-8244

Authors

Hauschild, Dirk

Seitz, Linsey

Gharibzadeh, Saba

et al.

Publication Date

2021-11-10

DOI

10.1021/acsami.1c15707

Impact of n-Butylammonium Bromide on the Chemical and Electronic Structure of Double-Cation Perovskite Thin Films

D. Hauschild[1,2,3,*], L. C. Seitz[1,#], S. Gharibzadeh[4,5], R. Steininger[1], N. Jiang[3], W. Yang[6], U. W. Paetzold[4,5], C. Heske[1,2,3], and L. Weinhardt[1,2,3,*]

[1] Institute for Photon Science and Synchrotron Radiation (IPS), Karlsruhe Institute of Technology (KIT), Germany

[2] Institute for Chemical Technology and Polymer Chemistry (ITCP), Karlsruhe Institute of Technology (KIT), Germany

[3] Department of Chemistry and Biochemistry, University of Nevada, Las Vegas (UNLV), Las Vegas, NV 89154, USA

[4] Institute of Microstructure Technology (IMT), Karlsruhe Institute of Technology (KIT), Germany

[5] Light Technology Institute (LTI), Karlsruhe Institute of Technology (KIT), Germany

[6] Advanced Light Source (ALS), Lawrence Berkeley National Laboratory, USA

*Authors to whom correspondence should be addressed: dirk.hauschild@kit.edu, lothar.weinhardt@kit.edu

Current address: Department of Chemical and Biological Engineering, Northwestern University, 2145 Sheridan Road, Evanston, IL 60208, USA

Abstract:

2D/3D perovskite heterostructures have emerged as a promising material composition to reduce non-radiative recombination in perovskite-based LEDs and solar cells. Such heterostructures can be created by a surface treatment with large organic cations, for example n-butylammonium bromide (BABr). To understand the impact of the BABr surface treatment on the double-cation ($Cs_{0.17}FA_{0.83}Pb(I_{0.6}Br_{0.4})_3$) (FA = formamidinium) perovskite thin film and to further optimize the corresponding structures, an in-depth understanding of the chemical and electronic properties of the involved surfaces, interfaces, and bulk is required. Hence, we study the impact of the BABr treatment with a combination of surface-sensitive x-ray photoelectron spectroscopy and bulk-sensitive resonant inelastic soft x-ray scattering (RIXS). A quantitative analysis of the BABr-treated perovskite thin film shows a modified chemical perovskite surface environment of carbon, nitrogen, bromine, iodine, and lead, indicating that the treatment leads to a perovskite surface with a modified composition and bonding structure. With K-edge RIXS, the local environment at the nitrogen and carbon atoms is probed, allowing us to identify the presence of BABr in the perovskite bulk, albeit with a modified bonding environment. This, in turn, identifies a “hidden parameter” for the optimization of the BABr treatment and the overall performance of 2D/3D perovskite solar-cell absorbers.

Keywords: photoelectron spectroscopy, resonant inelastic soft x-ray scattering, x-ray emission spectroscopy, x-ray absorption spectroscopy, perovskite-based solar cells, n-butylammonium bromide surface treatment, 2D/3D perovskite heterostructure

Introduction

Over the last decade, organic–inorganic hybrid perovskite-based optoelectronic devices and, in particular, solar cells (PSCs) have attracted enormous interest. With a rapid increase, the power conversion efficiency (PCE) of PSCs on laboratory scale has now surpassed those of the established polycrystalline Si, Cu(In,Ga)(S,Se)$_2$, and CdTe technologies, with a record PCE exceeding 25 %.[1] Moreover, wide-bandgap perovskite-based tandem solar cells have also achieved promising results.[2–4] PSCs are simple to process, as they are compatible with large-scale solution processing (e.g., roll-to-roll printing) and use abundant elements.[5]

However, the application of PSCs is hampered by their low stability under ambient conditions[6–9] and the fact that the best devices contain lead. [10,11] Significant improvements are necessary to achieve the goal of limiting efficiency losses to about 1 % (or less) per year over a lifetime of more than twenty years. A promising strategy to increase the stability of PSCs (and other solar cell parameters like the open-circuit voltage, V_{OC}) is to incorporate a 2D structure into the 3D perovskite[12–14]. Such 2D/3D perovskite can have a better crystalline quality than their 3D counterparts and could act as a protective layer against moisture.[15] In addition, reduced non-radiative recombination at the 2D/3D perovskite interface and an increase of the band gap is reported.[12] 2D/3D perovskite heterostructures are realized by a post treatment of the bulk 3D perovskite layer with large organic cations.

As we demonstrated in our earlier work, n-butylammonium bromide (BABr) can be readily used for such a surface treatment of double-cation wide bandgap perovskite absorbers ($Cs_{0.17}FA_{0.83}Pb(I_{0.6}Br_{0.4})_3$) (FA = formamidinium, $CH_5N_2^+$), resulting in a 2D/3D perovskite heterostructure.[16] This approach leads to PSCs with improved stability, efficiencies up to 19.4 %, and an enhanced V_{OC} of 1.31 V. In addition, other large organic cations were successfully explored to create 2D/3D perovskite heterostructures with enhanced solar-cell properties.[17–20]

In all of these surface treatments, the underlying processes are not fully understood; in particular, the interface modification upon BABr treatment needs to be investigated in more detail, as the interface constitutes a crucial component of the completed device. Our initial x-ray photoelectron spectroscopy (XPS) measurements suggest an increase of carbon, nitrogen, and bromine, i.e., BABr-related signals at the surface.[16] Ultraviolet photoelectron spectroscopy (UPS) measurements have highlighted a substantial spectral difference of the valence-band region and an additional downward band bending (by 0.12 eV) due to the BABr-treatment.[16] To further optimize and enhance the BABr surface treatment, an in-depth knowledge of its impact on the chemical and electronic properties of the surfaces, interfaces, *and bulk* of the 2D/3D perovskite heterostructure is required.

We thus have extended our previous XPS analysis of the surface modifications induced by the BABr surface treatment. In addition, we complement the surface-sensitive electron spectroscopy results with insights from bulk-sensitive soft x-ray spectroscopy techniques, i.e., x-ray absorption spectroscopy (XAS), x-ray emission spectroscopy (XES), and resonant inelastic soft x-ray scattering (RIXS) and are able to develop a depth-resolved chemical and electronic picture of the 2D/3D perovskite heterostructure.

Experimental

A detailed description of the sample preparation procedure can be found in Ref. 16 For the XPS study, two sets of $Cs_{0.17}FA_{0.83}Pb(I_{0.6}Br_{0.4})_3$ perovskite absorbers were prepared on a SnO_2/InSnO(ITO)/glass substrate by a one-step spin-coating process and subsequently annealed. Afterwards, the first set remained untreated (in the following referred to as "perovskite"), while n-butylammonium bromide (BABr) was dissolved in isopropanol (concentration 2 mg/mL) and spin-coated onto the second set of perovskite absorbers and subsequently annealed at 100°C for 5 min[16] to achieve a 2D/3D perovskite heterostructure (in the following referred to as "BABr/perovskite"). The entire sample processing and subsequent packaging was conducted in inert atmosphere. The samples were then transferred into the ultra-high vacuum (UHV) chamber used for XPS analysis within less than 1 h and without any air exposure.

All XPS measurements were performed using a non-monochromatized DAR 450 twin anode x-ray source (Omicron), providing Mg and Al K_α radiation, and an Argus CU electron analyzer (Omicron). Possible beam-induced changes to the films, leading to corresponding changes in the spectra, were estimated with short (1 and 11 min) measurements. From these measurements (see Supporting Information and Figure S1 for details), we concluded that the accumulated influence of beam-induced changes is acceptable within the first ~10 minutes of the XPS measurement, and thus all presented XPS spectra were collected within 10 minutes. To improve statistics and ensure reproducibility, the spectra of at least three identical samples were averaged. The XPS energy scale was calibrated using Ar^+ sputter-cleaned gold, copper, and silver foils, according to Ref. 21.

For the RIXS experiments, another (nominally identical) set of "perovskite" and "BABr/perovskite" samples was prepared. In addition, a BABr reference layer was spin-coated onto a glass substrate. The samples were shipped under inert atmosphere to Beamline 8.0.1 of the Advanced Light Source (ALS), Lawrence Berkeley National Lab. The RIXS measurements were performed with the SALSA endstation[22] and its high-transmission soft x-ray spectrometer.[23] The excitation and emission photon energy scales were calibrated with reference XAS measurements of N_2,[24] highly ordered pyrolytic graphite (HOPG),[25] and TiO_2,[26] as well as using elastically scattered Rayleigh lines, respectively.

Prior to this study, an upper limit of x-ray exposure time for any given sample spot was determined, as discussed in the Supporting Information in conjunction with Figure S2. As expected, soft x-rays from a high-flux-density beamline rapidly damage the perovskite material. To minimize this damage to a negligible level, rapid raster-scanning of the sample under the soft x-ray beam is necessary. As shown in the Supporting information and Figure S2, a speed of 600 µm/s (which corresponds to an exposure time of 50 ms for a given sample spot) was determined to be suitable.

Results

In our recent qualitative XPS evaluation of the surface chemical structure, we found distinct changes upon BABr treatment,[16] in particular a decrease of the I, Pb, and Cs signals, but no change of the peak shapes. This suggests the absence of significant changes in the chemical environments of these elements. In contrast, the N 1s, C 1s, and Br 3d signals not only showed clear intensity increases (as expected for a BABr treatment), but also changes in their peak *shapes*, which have not been analyzed in our previous study.

Accordingly, to gain a more detailed and, in particular, quantitative picture, these changes were analyzed by fitting the photoelectron signals (i.e., N 1s, C 1s, and Br 3d) of the $Cs_{0.17}FA_{0.83}Pb(I_{0.6}Br_{0.4})_3$ layer before and after the BABr treatment, as shown in Figure 1. The spectra for each core level were fitted simultaneously, using a linear background and a minimal number of Voigt profiles with coupled widths, fixed peak distances, and, according to the 2j+1 multiplicity, the appropriate 4:6 ratio for the Br 3d spin-orbit doublet.

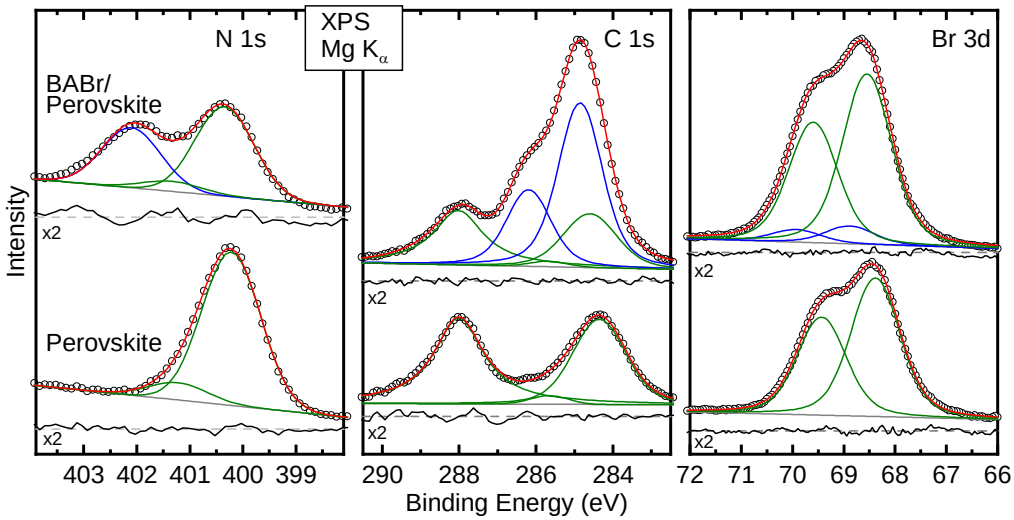

Figure 1. XPS Mg K_α spectra of the N 1s, C 1s, and Br 3d core levels of perovskite (bottom) and BABr/perovskite (top). Experimental data is depicted as open circles, fit results as solid red lines. The individual fit components of the perovskite sample are shown in green. Additional components found after the BABr surface treatment are shown in blue. The residuals are shown below the fits and are magnified by a factor of 2.

The N 1s signal of the perovskite consists of one main feature at ~400.2 eV, which can be assigned to the amidinium functional group in the FA molecule.[3,27–29] In addition, the spectrum shows a slight asymmetry towards higher binding energies. To describe this, we have used a second Voigt function at ~401.3 eV. Possible origins for this (weak) component might be shortcomings of using a linear background[30] in the fit, contributions from the neighboring Pb $4d_{5/2}$ core level excited by Mg K_α x-ray satellite lines,[31] asymmetric vibronic broadening,[32] and/or an additional chemical nitrogen species.[33,34]

For the N 1s spectrum of the BABr/perovskite sample, a new peak at ~402.1 eV, ascribed to the nitrogen atom of the $–NH_3^+$ functional group of the BABr molecule. For the fit, the separation and ratio of the two FA-related fit peaks were kept constant. We observe an intensity decrease of the FA-related peaks by ~40 %, and a slight shift to higher binding energies.

The C 1s signal of the perovskite shows two main features, at ~284.4 and ~288.0 eV, respectively. Additional intensity in the “valley” between these two features can be described by a third component at ~285.8 eV. A similar C 1s spectral structure has previously been reported for FA-based perovskites[28]. An intact FA molecule features only one carbon environment, and we would thus expect only one C 1s component. A comparison with literature[27,34] suggests that the high binding-energy peak at ~288.0 eV should be assigned to carbon in the intact FA environment ($-CN_2H_4^+$). This assignment is supported by the

XPS-derived ratio between N and C (only using the C 1s peak at ~288.0 eV) of (1.8 ± 0.3):1, which fits to the expected ratio of 2:1. The signal at ~284.4 eV is commonly ascribed to carbon in a $–CH_3^+$ environment and assigned to a "defect-type" species[35]. In a similar fashion, we tentatively assign the small peak at ~285.5 eV to a defect-type C-N^+ species.[33,35] We point out that the oxygen signal at the surface is very small (see survey spectrum in Ref. 16), which rules out a significant contribution of C-O bonds to the C 1s spectrum.

Upon BABr treatment, the spectral signature of the C 1s region changes, and two additional Voigt functions at ~284.9 and ~286.2 eV (with identical shape and width) are needed for a complete description of the spectrum. The feature at ~286.2 eV is assigned to the carbon atom attached to the $–NH_3^+$ functional group, while the peak at ~284.9 eV is attributed to the butyl part of the BABr molecule.[21] In parallel, the intensities of the C 1s perovskite peaks are attenuated by ~30 % (note that the attenuation behavior will be discussed below in conjunction with Figure 2).

The Br 3d signal of the perovskite can be described by a single spin-orbit doublet, with the Br $3d_{5/2}$ peak at ~68.4 eV, attributed to bromine in the perovskite crystal structure.[36] Upon BABr treatment, the total Br 3d intensity increases by 35 %, and an additional Br 3d doublet appears at ~68.9 eV; its fraction of the total Br 3d intensity is ~10 %. The additional Br species could stem from the Br atom in a BABr environment, or the integration of Br into the perovskite in a different chemical environment. Also, the formation of a secondary phase, e.g., with Pb-Br bonds (reported at a binding energy of 68.7 ± 0.2 eV[27]), cannot be excluded.

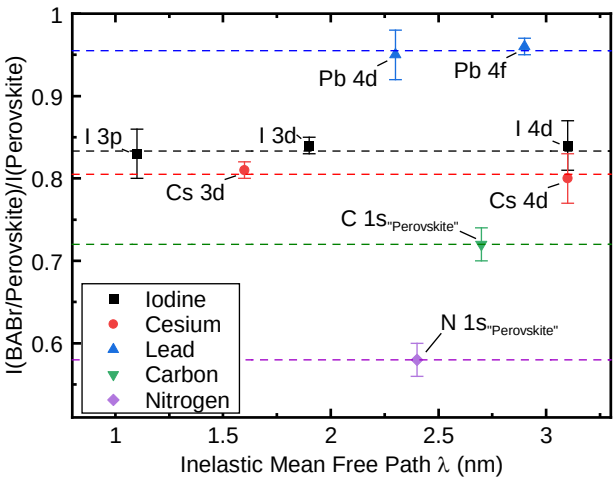

Figure 2. Intensity ratio I(BABr/perovskite)/I(perovskite) of different perovskite core-level lines as a function of the inelastic mean free path (IMFP) λ. Horizontal dashed lines indicate the average ratio for each element.

To further expand our previous qualitative XPS analysis[16], the quantitative composition at the BABr/perovskite surface was determined using the intensity ratios I(BABr/perovskite)/I(perovskite) of prominent core-level lines of lead (blue), iodine (black), and cesium (red), as well as the perovskite component of the C 1s (green) and N 1s (purple) lines. As mentioned, the corresponding fits are shown in Figure 1. The ratios are plotted in Figure 2 as a function of the inelastic mean free path (IMFP) λ of the corresponding photoelectrons. λ gives the 1/e attenuation length of a beam of (photo-)electrons and

varies as a function of kinetic energy, thus determining (and allowing for small variations in) the surface sensitivity of XPS.

Here, the IMFP was determined from the respective kinetic energy of the core-level lines using QUASES-IMFP[37] (based on Ref. [38]). Within the error bars, the derived intensity ratios are identical for a given element, *independent* of the IMFP, and differ strongly between the different elements. In detail, we find values of 0.96, 0.84, and 0.81 (± 0.01), for lead, iodine, and cesium, respectively. The values for the perovskite component in the carbon and the nitrogen core levels are 0.72 and 0.58, respectively. The fact that the intensity ratios for a given element are independent of the IMFP rules out a simple A-on-B layer structure, i.e., with a thin BABr layer on top of the 3D perovskite bulk layer. Rather, it suggests the formation of a modified outermost surface region that is homogeneous within the region probed by XPS, with a composition different from both BABr and the 3D perovskite. Ultimately, all of the perovskite elements in Figure 2 are reduced in surface concentration after the BABr treatment, most strongly perovskite N and C, followed by Cs, I, and Pb. In contrast, non-perovskite N and C, as well as Br, increase in surface concentration. Accordingly, we speculate that some of the FA and I might be replaced by BA and Br, respectively.

Upon BABr treatment, we thus find that a "new" perovskite surface layer is formed, with a different composition compared to the perovskite surface, and with additional chemical environments for carbon, nitrogen, and bromine.

Further insights into the impact of BABr on the chemical and electronic structure of the 3D perovskite bulk layer can be gained using RIXS and non-resonant XES. As "photon-in photon-out" soft x-ray techniques, they offer an increased 1/e attenuation length in both BABr and perovskite (~150 – 300 nm[39]), thus probing the majority of the ~400 nm thick[16] perovskite samples. Furthermore, RIXS and XES are element-specific local probes of the electronic structure around the core-excited atom. Here, we collected N and C K RIXS maps[23,40–42] and non-resonant XES spectra to investigate the occupied and unoccupied electronic structure at the nitrogen and carbon atoms of the perovskite, the BABr/perovskite, and a BABr reference sample.

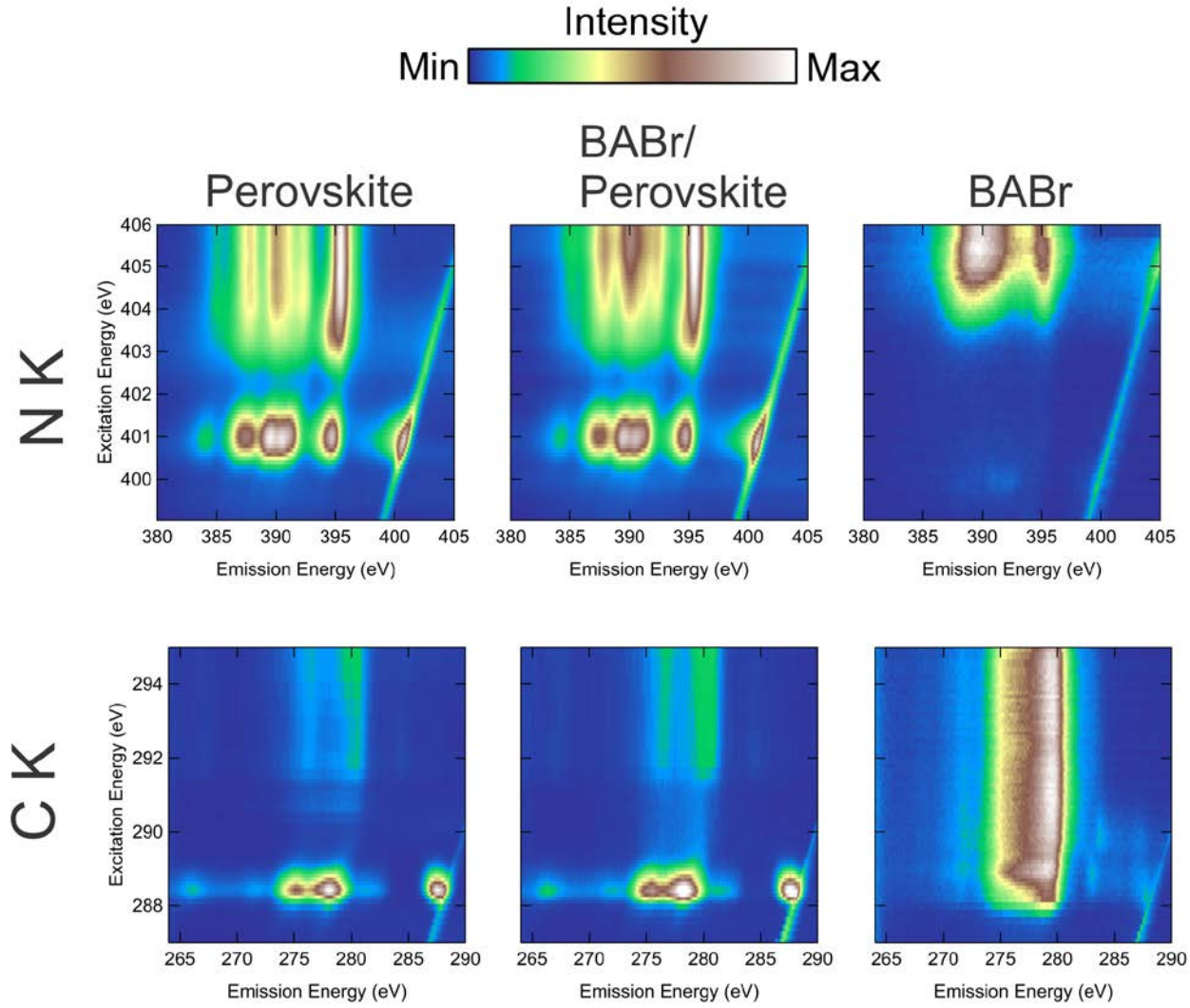

Figure 3. N (top) and C (bottom) K RIXS maps of the $Cs_{0.17}FA_{0.83}Pb(I_{0.6}Br_{0.4})_3$ perovskite (left), BABr/perovskite (center), and a BABr reference (right). In the RIXS maps, the x-ray emission intensity is color-coded and shown as a function of excitation and emission energy.

In the RIXS maps shown in Figure 3, the x-ray emission intensity is color-coded and depicted as a function of the excitation (ordinate) and emission energy (abscissa). At first glance, the respective perovskite and BABr/perovskite RIXS maps are very similar, while the BABr RIXS maps differ significantly for both N and C K.

For a better understanding, all maps can be separated into “spectator” and “participant” emission regions. For the N (C) maps, the former is found for emission energies below ~397 eV (~285 eV), while the latter is found above these values. The participant region includes the Rayleigh line, appearing as a diagonal in the map, at equal emission and excitation energies. Loss structures at excitation energies of ~401.0 and ~288.4 eV can be clearly detected close to the Raleigh line, for both the perovskite and the BABr/perovskite samples (but not the BABr reference).

To understand the electronic structure signatures in the RIXS maps in more detail, we first analyze the non-resonant XES spectra at excitation energies of 320 and 420 eV for C and N K, respectively. The corresponding C (left) and N (right) spectra for the $Cs_{0.17}FA_{0.83}Pb(I_{0.6}Br_{0.4})_3$ perovskite (black), the BABr/perovskite (red), and the BABr reference (blue) samples are shown in Figure 4. In addition, the difference between the spectra of the BABr/perovskite sample and the perovskite are shown in green (multiplied by 0.5). Further analysis of the RIXS maps will then follow in conjunction with Figures 5 and 6.

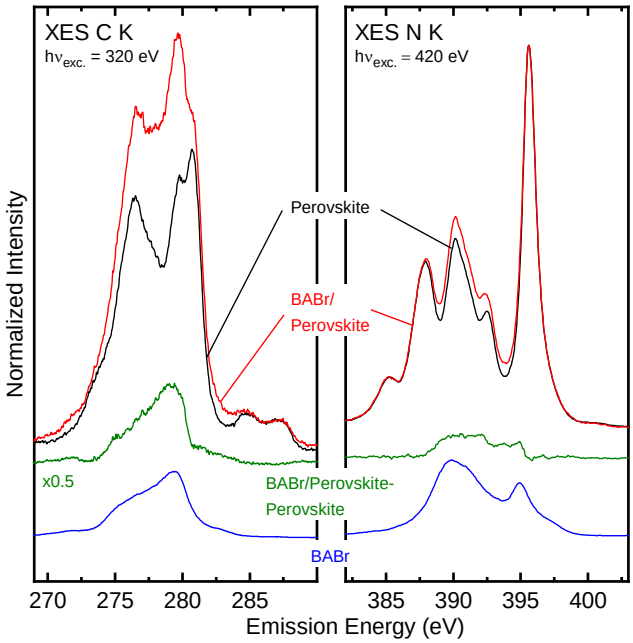

Figure 4. Non-resonant C ($h\nu_{exc.}$ = 320 eV, left) and N ($h\nu_{exc.}$ = 420 eV, right) K-edge XES spectra of the perovskite (black), BABr/perovskite (red), and BABr reference (blue) sample. The difference between the spectra of the BABr/perovskite sample and the perovskite is shown in green (x 0.5).

In Figure 4, we find that the spectral fingerprints of the perovskite sample (i.e., of FA) and the BABr reference (i.e., of BA) are very distinct and give a characteristic probe for the respective bonding environments. Specifically, the N K emission of perovskite and BABr/perovskite (i.e., the fingerprint of the amidinium functional group) shows an intense peak at 395.6 eV, which is clearly separated from the rest of the spectrum, and a number of weaker close-lying peaks between 384 and 394 eV. We attribute the peak at 395.6 eV to transitions involving the nitrogen lone pair orbitals, as they were also identified in the neutral amino groups ($–NH_2$) of amino acids,[40,43] and the features between 384 and 394 eV to transitions from lower-lying valence orbitals into the N 1s core hole. The spectrum of the BABr reference consist of a broad structure around 390 eV and a sharp peak at 395.0 eV. This signature can be related to a protonated amino group ($–NH_3^+$),[40,44] as present in BA.

Blum *et al.*[40] found that the NH_3^+ group undergoes ultra-fast dissociation on the time-scale of the x-ray emission process after x-ray excitation. While the broad signal at ~390 eV stems from x-ray emission of the intact NH_3^+ group, the peak at 395 eV can be attributed to emission after dissociation, leaving a neutral amino group after the removal of a proton.

The N K XES spectrum of BABr/perovskite (shown in red) is dominated by the signal from the FA environment. A difference spectrum was computed by subtracting the spectral contribution of the perovskite from the BABr/perovskite spectrum and is shown in green in Figure 4. We find that this difference spectrum resembles the BA signature.

The non-resonant C K XES measurements of the perovskite, the BABr/perovskite, and the BABr reference (Figure 4, left) also show substantial changes induced by the BABr treatment. For the perovskite sample (i.e., the FA fingerprint), we find a broad peak around 276.4 eV, a double-peak feature at 279.8 and 280.7 eV, and two broader less-intense features at 285.0 and 287.5 eV. Again, the BABr spectrum looks distinctively different, with a maximum at ~279 eV and a broad shoulder that extends to ~274 eV. By subtracting the perovskite spectrum from that of the BABr/perovskite sample, the spectral signature of the BABr reference can clearly be detected, as shown in green in Figure 4. The non-resonant XES spectra thus suggest that the newly formed perovskite layer of the BABr/perovskite sample, as observed in XPS, contains both FA and BA, and that these stay "intact" when compared to their individual references.

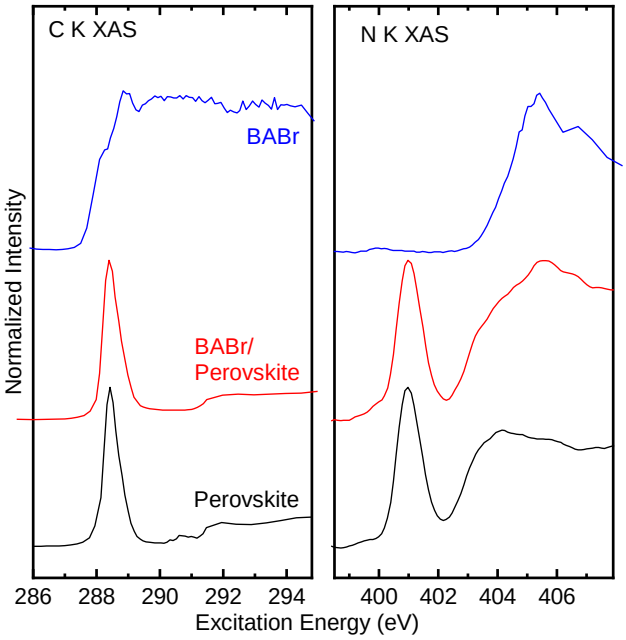

Figure 5. Partial fluorescence yield C (left, emission integrated between 265 – 285 eV) and N (right, emission integrated between 380 – 397 eV) K-edge XAS spectra of the perovskite (black), BABr/perovskite (red), and BABr reference (blue).

Integrating each emission spectrum in the N K RIXS maps between 380 and 397 eV (i.e., the spectator emission), partial fluorescence yield (PFY) XAS spectra are computed and shown in the right panel of Figure 5. For the perovskite sample, a prominent first resonance at ~401 eV is found. A comparison with literature[40,43,45] suggests that this resonance can be attributed to an N 1s → π* transition at the amidinium group. In contrast, this resonance is not visible for the BABr reference and its protonated amino group. For excitation energies larger than ~402 eV (for the perovskite) and ~403 eV (for the BABr reference), respectively, a broad structure with some individual finer features is found, which is ascribed to N 1s →

σ* transitions.[46,47] The spectrum of the BABr/perovskite sample (red in Figure 5) again resembles a superposition of the spectra of the perovskite sample and the BABr reference.

In the same fashion as at the N K edge, C K PFY XAS spectra were extracted from the C K maps between 265 and 285 eV) and are shown in the left panel in Figure 5. The C K XAS spectrum of the perovskite is dominated by a strong resonance at 288.4 eV, with a slight asymmetry towards higher excitation energies. We attribute this resonance to C 1s → π* transitions at the amidinium functional group, in accordance with similar features found for compounds involving C=N bonds.[47] At ~291 eV, we find the much weaker C 1s → σ* transitions.[46] In contrast, no π* resonances are expected for BABr, and the absorption spectrum consequently does not show any strong resonance, but only some weaker variations around the absorption edge at ~288 eV. The rather featureless structure of the spectrum can be attributed to a multitude of overlapping C 1s → σ* transitions in the different bonding environments of BA (C-H, C-C, and C-N).[46–49] Due to the weak and rather featureless signature of the BA C K spectrum, its signature cannot be clearly identified in the spectrum of the BABr/perovskite sample, which is strongly dominated by the perovskite contribution.

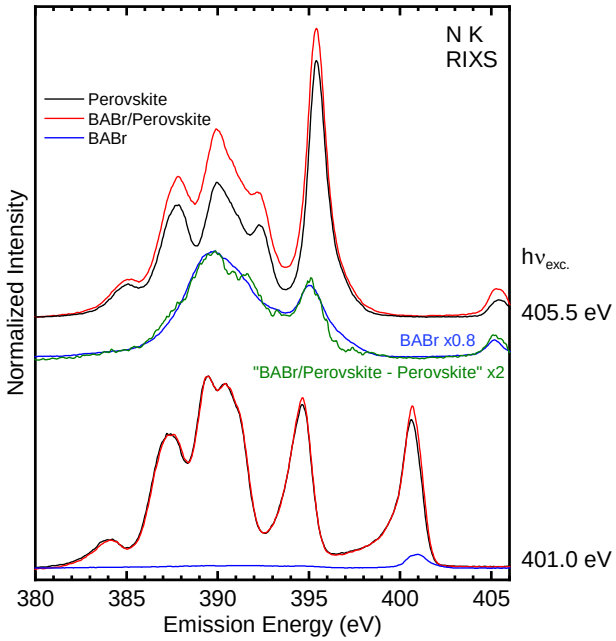

Figure 6. N K RIXS spectra of perovskite, BABr/perovskite, and BABr, excited at 401.0 ± 0.5 eV (bottom) and 405.5 ± 0.5 eV (top). At 401.0 eV, no intensity is observed for the BABr spectrum. For the 405.5 eV spectra, the magnified difference spectrum "BABr/perovskite – perovskite" (green, x2) is also shown, overlayed with the BABr spectrum (x0.8).

Resonant XES spectra were extracted from the N K RIXS maps at excitation energies of 401 and 405.5 eV, as shown in Figure 6 bottom and top, respectively. Since no significant spectral variations were observed, the spectra within ±0.5 eV around these excitation energies were summed up to improve the signal-to-noise ratio. At an excitation energy of 401 eV, only the FA molecule is excited, and no emission is observed for the pure BABr sample, except for a small peak at an emission energy of 401 eV that corresponds to the Rayleigh line. For the perovskite and BABr/perovskite, i.e., the FA-containing samples,

a strong feature at 394.6 eV can be related to transitions involving the nitrogen lone-pair orbital. Compared to the spectra excited at 405.5 and 420 eV (see also Figure 4), this emission line exhibits a "spectator shift"[50] by -1.0 eV, and its relative intensity decreases.

At 405.5 eV excitation energy, the spectra of the perovskite and BABr/perovskite samples differ mainly in the region between 386 – 394 eV (Figure 6 top). To identify the spectral contributions of the BA molecule, a difference spectrum "BABr/perovskite – perovskite" is calculated (green, magnified x2). This difference resembles the general structure of the BABr reference spectrum, which is shown for comparison. However, at an emission energy of ~396.5 eV, a small difference is observed, namely a lower intensity in the difference spectrum. As discussed above for the non-resonant spectra, this energy region is influenced by dissociation of the NH_3^+ group on the time-scale of the RIXS process[40]. The dissociation process is very sensitive to the chemical surrounding of the respective functional group, as was observed for, e.g., liquid water[51], ammonia[52,53], and salt solutions[54,55]. Thus, we assign the differences to a different bonding environment of the BA molecule in the BABr/perovskite sample, compared to that in the BABr reference. Nevertheless, the BABr signature suggests that the molecule remains intact, and hence we interpret this result such that BABr is incorporated into a 2D/3D perovskite structure, as opposed to forming a separate BABr secondary phase. This corroborates our previous results[16], which identified the formation of 2D perovskite interlayers for BABr surface treatments of the $Cs_{0.17}FA_{0.83}Pb(I_{0.6}Br_{0.4})_3$ perovskite absorber layer.

Overall, the RIXS, XES, and XAS data thus suggest that both, the FA and BA moieties, stay intact during and after the BABr treatment, and that the resulting surface is characterized by the presence of a newly formed perovskite layer with modified composition that contains both FA and BA molecules in their original form.

Summary

We have studied the impact of an n-butylammonium bromide (BABr) surface treatment on the chemical and electronic structure of a $Cs_{0.17}FA_{0.83}Pb(I_{0.6}Br_{0.4})_3$ perovskite using surface-sensitive XPS and bulk-sensitive XES and RIXS. Our XPS data reveals additional components in the C 1s, N 1s, and Br 3d spectrum after the treatment, which can be related to the addition of BA^+ and Br^- ions to the surface layer. A detailed quantitative analysis of all perovskite-related lines highlights a change in surface composition, which suggests the formation of a "new" perovskite layer at the outermost surface with a changed stoichiometry. With XES and RIXS at the N K and C K edges, a more bulk-sensitive view reveals a clear spectral identification of the formamidinium and butylammonium ions. The spectra of the BABr/perovskite sample suggest that both FA and BA ions stay intact and are present in the newly-formed surface layer. Moreover, our spectra suggest a change in local chemical environment of the BA in the perovskite compared to the BABr reference, impacting the ultrafast dissociation behavior in our RIXS spectrum, in agreement with the formation of a 2D/3D perovskite heterostructure.

Overall, thus, we identify and clarify a "hidden" parameter, namely the presence and local environment of the BA molecule in the modified perovskite surface after the BABr surface treatment. We speculate that this parameter is also crucial for other 2D/3D perovskite heterostructures as well, which will allow for a deliberate optimization of such treatments and thus the overall performance of perovskite solar-cell devices.

Acknowledgements

We gratefully acknowledge the Deutsche Forschungsgemeinschaft (DFG) for funding of the MFE lab instrumentation in project GZ:INST 121384/64-1 FUGG. L.S. thanks funding by the German Helmholtz-Association in the framework of the Helmholtz postdoctoral fellowship program (Grant No. PD-326). This research used resources of the Advanced Light Source, which is a DOE Office of Science User Facility under contract no. DE-AC02-05CH11231.

Supporting Information

Influence of beam-induced changes on XPS and XES spectra

References

(1) Best Research-Cell Efficiency Chart | Photovoltaic Research | NREL https://www.nrel.gov/pv/cell-efficiency.html (accessed 2021 -05 -25).

(2) Jošt, M.; Bertram, T.; Koushik, D.; Marquez, J. A.; Verheijen, M. A.; Heinemann, M. D.; Köhnen, E.; Al-Ashouri, A.; Braunger, S.; Lang, F.; Rech, B.; Unold, T.; Creatore, M.; Lauermann, I.; Kaufmann, C. A.; Schlatmann, R.; Albrecht, S. 21.6%-Efficient Monolithic Perovskite/Cu(In,Ga)Se_2 Tandem Solar Cells with Thin Conformal Hole Transport Layers for Integration on Rough Bottom Cell Surfaces. *ACS Energy Lett.* **2019**, *4* (2), 583–590. https://doi.org/10.1021/acsenergylett.9b00135.

(3) Nejand, B. A.; Hossain, I. M.; Jakoby, M.; Moghadamzadeh, S.; Abzieher, T.; Gharibzadeh, S.; Schwenzer, J. A.; Nazari, P.; Schackmar, F.; Hauschild, D.; Weinhardt, L.; Lemmer, U.; Richards, B. S.; Howard, I. A.; Paetzold, U. W. Vacuum-Assisted Growth of Low-Bandgap Thin Films ($FA_{0.8}MA_{0.2}Sn_{0.5}Pb_{0.5}I_3$) for All-Perovskite Tandem Solar Cells. *Adv. Energy Mater.* **2020**, *10* (5), 1902583. https://doi.org/10.1002/aenm.201902583.

(4) Sahli, F.; Werner, J.; Kamino, B. A.; Bräuninger, M.; Monnard, R.; Paviet-Salomon, B.; Barraud, L.; Ding, L.; Diaz Leon, J. J.; Sacchetto, D.; Cattaneo, G.; Despeisse, M.; Boccard, M.; Nicolay, S.; Jeangros, Q.; Niesen, B.; Ballif, C. Fully Textured Monolithic Perovskite/Silicon Tandem Solar Cells with 25.2% Power Conversion Efficiency. *Nat. Mater.* **2018**, *17* (9), 820–826. https://doi.org/10.1038/s41563-018-0115-4.

(5) Yang, D.; Yang, R.; Priya, S.; Liu, S. (Frank). Recent Advances in Flexible Perovskite Solar Cells: Fabrication and Applications. *Angew. Chem. Int. Ed.* **2019**, *58* (14), 4466–4483. https://doi.org/10.1002/anie.201809781.

(6) Wang, R.; Mujahid, M.; Duan, Y.; Wang, Z.-K.; Xue, J.; Yang, Y. A Review of Perovskites Solar Cell Stability. *Adv. Funct. Mater.* **2019**, *29* (47), 1808843. https://doi.org/10.1002/adfm.201808843.

(7) Kim, S.; Bae, S.; Lee, S.-W.; Cho, K.; Lee, K. D.; Kim, H.; Park, S.; Kwon, G.; Ahn, S.-W.; Lee, H.-M.; Kang, Y.; Lee, H.-S.; Kim, D. Relationship between Ion Migration and Interfacial Degradation of $CH_3NH_3PbI_3$ Perovskite Solar Cells under Thermal Conditions. *Sci. Rep.* **2017**, *7* (1), 1–9. https://doi.org/10.1038/s41598-017-00866-6.

(8) Farooq, A.; Hossain, I. M.; Moghadamzadeh, S.; Schwenzer, J. A.; Abzieher, T.; Richards, B. S.; Klampaftis, E.; Paetzold, U. W. Spectral Dependence of Degradation under Ultraviolet Light in Perovskite Solar Cells. *ACS Appl. Mater. Interfaces* **2018**, *10* (26), 21985–21990. https://doi.org/10.1021/acsami.8b03024.

(9) Boyd, C. C.; Cheacharoen, R.; Leijtens, T.; McGehee, M. D. Understanding Degradation Mechanisms and Improving Stability of Perovskite Photovoltaics. *Chem. Rev.* **2019**, *119* (5), 3418–3451. https://doi.org/10.1021/acs.chemrev.8b00336.

(10) Clever, H. L.; Johnston, F. J. The Solubility of Some Sparingly Soluble Lead Salts: An Evaluation of the Solubility in Water and Aqueous Electrolyte Solution. *J. Phys. Chem. Ref. Data* **1980**, *9* (3), 751. https://doi.org/10.1063/1.555628.

(11) Fu, H. Review of Lead-Free Halide Perovskites as Light-Absorbers for Photovoltaic Applications: From Materials to Solar Cells. *Sol. Energy Mater. Sol. Cells* **2019**, *193*, 107–132. https://doi.org/10.1016/j.solmat.2018.12.038.

(12) Stoumpos, C. C.; Cao, D. H.; Clark, D. J.; Young, J.; Rondinelli, J. M.; Jang, J. I.; Hupp, J. T.; Kanatzidis, M. G. Ruddlesden–Popper Hybrid Lead Iodide Perovskite 2D Homologous Semiconductors. *Chem. Mater.* **2016**, *28* (8), 2852–2867. https://doi.org/10.1021/acs.chemmater.6b00847.

(13) Etgar, L. The Merit of Perovskite's Dimensionality; Can This Replace the 3D Halide Perovskite? *Energy Environ. Sci.* **2018**, *11* (2), 234–242. https://doi.org/10.1039/C7EE03397D.

(14) Ke, W.; Mao, L.; Stoumpos, C. C.; Hoffman, J.; Spanopoulos, I.; Mohite, A. D.; Kanatzidis, M. G. Compositional and Solvent Engineering in Dion–Jacobson 2D Perovskites Boosts Solar Cell Efficiency and Stability. *Adv. Energy Mater.* **2019**, *9* (10), 1803384. https://doi.org/10.1002/aenm.201803384.
(15) Grancini, G.; Roldán-Carmona, C.; Zimmermann, I.; Mosconi, E.; Lee, X.; Martineau, D.; Narbey, S.; Oswald, F.; Angelis, F. D.; Graetzel, M.; Nazeeruddin, M. K. One-Year Stable Perovskite Solar Cells by 2D/3D Interface Engineering. *Nat. Commun.* **2017**, *8* (1), 1–8. https://doi.org/10.1038/ncomms15684.
(16) Gharibzadeh, S.; Nejand, B. A.; Jakoby, M.; Abzieher, T.; Hauschild, D.; Moghadamzadeh, S.; Schwenzer, J. A.; Brenner, P.; Schmager, R.; Haghighirad, A. A.; Weinhardt, L.; Lemmer, U.; Richards, B. S.; Howard, I. A.; Paetzold, U. W. Record Open-Circuit Voltage Wide-Bandgap Perovskite Solar Cells Utilizing 2D/3D Perovskite Heterostructure. *Adv. Energy Mater.* **2019**, *9* (21), 1803699. https://doi.org/10.1002/aenm.201803699.
(17) Luo, D.; Yang, W.; Wang, Z.; Sadhanala, A.; Hu, Q.; Su, R.; Shivanna, R.; Trindade, G. F.; Watts, J. F.; Xu, Z.; Liu, T.; Chen, K.; Ye, F.; Wu, P.; Zhao, L.; Wu, J.; Tu, Y.; Zhang, Y.; Yang, X.; Zhang, W.; Friend, R. H.; Gong, Q.; Snaith, H. J.; Zhu, R. Enhanced Photovoltage for Inverted Planar Heterojunction Perovskite Solar Cells. *Science* **2018**, *360* (6396), 1442–1446. https://doi.org/10.1126/science.aap9282.
(18) Cho, Y.; Soufiani, A. M.; Yun, J. S.; Kim, J.; Lee, D. S.; Seidel, J.; Deng, X.; Green, M. A.; Huang, S.; Ho-Baillie, A. W. Y. Mixed 3D–2D Passivation Treatment for Mixed-Cation Lead Mixed-Halide Perovskite Solar Cells for Higher Efficiency and Better Stability. *Adv. Energy Mater.* **2018**, *8* (20), 1703392. https://doi.org/10.1002/aenm.201703392.
(19) Cho, K. T.; Grancini, G.; Lee, Y.; Oveisi, E.; Ryu, J.; Almora, O.; Tschumi, M.; Schouwink, P. A.; Seo, G.; Heo, S.; Park, J.; Jang, J.; Paek, S.; Garcia-Belmonte, G.; Nazeeruddin, M. K. Selective Growth of Layered Perovskites for Stable and Efficient Photovoltaics. *Energy Environ. Sci.* **2018**, *11* (4), 952–959. https://doi.org/10.1039/C7EE03513F.
(20) Yoo, J. J.; Wieghold, S.; Sponseller, M. C.; Chua, M. R.; Bertram, S. N.; Hartono, N. T. P.; Tresback, J. S.; Hansen, E. C.; Correa-Baena, J.-P.; Bulović, V.; Buonassisi, T.; Shin, S. S.; Bawendi, M. G. An Interface Stabilized Perovskite Solar Cell with High Stabilized Efficiency and Low Voltage Loss. *Energy Environ. Sci.* **2019**, *12* (7), 2192–2199. https://doi.org/10.1039/C9EE00751B.
(21) Moulder, J. F.; Stickle, W. F.; Sobol, P. E.; Bomben, K. D. *Handbook of X-Ray Photoelectron Spectroscopy, Perkin-Elmer Corporation.*; Physical Electronics Division, 1992.
(22) Blum, M.; Weinhardt, L.; Fuchs, O.; Bär, M.; Zhang, Y.; Weigand, M.; Krause, S.; Pookpanratana, S.; Hofmann, T.; Yang, W.; Denlinger, J. D.; Umbach, E.; Heske, C. Solid and Liquid Spectroscopic Analysis (SALSA)–a Soft x-Ray Spectroscopy Endstation with a Novel Flow-through Liquid Cell. *Rev. Sci. Instrum.* **2009**, *80* (12), 123102. https://doi.org/10.1063/1.3257926.
(23) Fuchs, O.; Weinhardt, L.; Blum, M.; Weigand, M.; Umbach, E.; Bär, M.; Heske, C.; Denlinger, J.; Chuang, Y.-D.; McKinney, W.; Hussain, Z.; Gullikson, E.; Jones, M.; Batson, P.; Nelles, B.; Follath, R. High-Resolution, High-Transmission Soft x-Ray Spectrometer for the Study of Biological Samples. *Rev. Sci. Instrum.* **2009**, *80* (6), 063103. https://doi.org/10.1063/1.3133704.
(24) Kato, M.; Morishita, Y.; Oura, M.; Yamaoka, H.; Tamenori, Y.; Okada, K.; Matsudo, T.; Gejo, T.; Suzuki, I. H.; Saito, N. Absolute Photoionization Cross Sections with Ultra-High Energy Resolution for Ar, Kr, Xe and N_2 in Inner-Shell Ionization Regions. *J. Electron Spectrosc. Relat. Phenom.* **2007**, *160* (1), 39–48. https://doi.org/10.1016/j.elspec.2007.06.003.
(25) Watts, B.; Ade, H. A Simple Method for Determining Linear Polarization and Energy Calibration of Focused Soft X-Ray Beams. *J. Electron Spectrosc. Relat. Phenom.* **2008**, *162* (2), 49–55. https://doi.org/10.1016/j.elspec.2007.08.008.

(26) Lusvardi, V. S.; Barteau, M. A.; Chen, J. G.; Eng, J.; Frühberger, B.; Teplyakov, A. An NEXAFS Investigation of the Reduction and Reoxidation of TiO_2(001). *Surf. Sci.* **1998**, *397* (1), 237–250. https://doi.org/10.1016/S0039-6028(97)00740-1.
(27) Naumkin, A.; Kraut-Vass, A.; Gaarenstroom, S.; Powell, C. NIST X-ray Photoelectron Spectroscopy (XPS) Database, Version 4.1 http://srdata.nist.gov/xps/Default.aspx (accessed 2021 -02 -14).
(28) Rodriguez-Pereira, J.; Tirado, J.; Gualdrón-Reyes, A. F.; Jaramillo, F.; Ospina, R. XPS of the Surface Chemical Environment of CsMAFAPbBrI Trication-Mixed Halide Perovskite Film. *Surf. Sci. Spectra* **2020**, *27* (2), 024003. https://doi.org/10.1116/6.0000275.
(29) Philippe, B.; Saliba, M.; Correa-Baena, J.-P.; Cappel, U. B.; Turren-Cruz, S.-H.; Grätzel, M.; Hagfeldt, A.; Rensmo, H. Chemical Distribution of Multiple Cation (Rb^+, Cs^+, MA^+, and FA^+) Perovskite Materials by Photoelectron Spectroscopy. *Chem. Mater.* **2017**, *29* (8), 3589–3596. https://doi.org/10.1021/acs.chemmater.7b00126.
(30) Hauschild, D.; Handick, E.; Göhl-Gusenleitner, S.; Meyer, F.; Schwab, H.; Benkert, A.; Pohlner, S.; Palm, J.; Tougaard, S.; Heske, C.; Weinhardt, L.; Reinert, F. Band-Gap Widening at the $Cu(In,Ga)(S,Se)_2$ Surface: A Novel Determination Approach Using Reflection Electron Energy Loss Spectroscopy. *ACS Appl. Mater. Interfaces* **2016**, *8* (32), 21101–21105. https://doi.org/10.1021/acsami.6b06358.
(31) Klauber, C. Magnesium K_α x-Ray Line Structure Revisited. *Appl. Surf. Sci.* **1993**, *70–71, Part 1*, 35–39. https://doi.org/10.1016/0169-4332(93)90393-P.
(32) Fronzoni, G.; Baseggio, O.; Stener, M.; Hua, W.; Tian, G.; Luo, Y.; Apicella, B.; Alfé, M.; de Simone, M.; Kivimäki, A.; Coreno, M. Vibrationally Resolved High-Resolution NEXAFS and XPS Spectra of Phenanthrene and Coronene. *J. Chem. Phys.* **2014**, *141* (4), 044313. https://doi.org/10.1063/1.4891221.
(33) Olthof, S.; Meerholz, K. Substrate-Dependent Electronic Structure and Film Formation of $MAPbI_3$ Perovskites. *Sci. Rep.* **2017**, *7*, 40267. https://doi.org/10.1038/srep40267.
(34) Zhou, Q.; Liang, L.; Hu, J.; Cao, B.; Yang, L.; Wu, T.; Li, X.; Zhang, B.; Gao, P. High-Performance Perovskite Solar Cells with Enhanced Environmental Stability Based on a $(p\text{-}FC_6H_4C_2H_3NH_3)_{\alpha 2}[PbI_4]$ Capping Layer. *Adv. Energy Mater.* **2019**, *9* (12), 1802595. https://doi.org/10.1002/aenm.201802595.
(35) Wang, R.; Zhuo, M.-P.; Li, J.; Zhai, T.; Yang, J.; Fu, K.; Liao, L.-S.; Liu, L.; Duhm, S. Surface $CH_3NH_3^+$ to CH_3^+ Ratio Impacts the Work Function of Solution-Processed and Vacuum-Sublimed $CH_3NH_3PbI_3$ Thin Films. *Adv. Mater. Interfaces* **2019**, *6* (6), 1801827. https://doi.org/10.1002/admi.201801827.
(36) Félix, R.; Rehermann, C.; Liu, D.; Handick, E.; Hartmann, C.; Wilks, R. G.; Unger, E.; Bär, M. Photoinduced Phase Segregation and Degradation of Perovskites Revealed by X-Ray Photoelectron Spectroscopy. In *2019 IEEE 46th Photovoltaic Specialists Conference (PVSC)*; 2019; pp 2362–2367. https://doi.org/10.1109/PVSC40753.2019.8980746.
(37) Tougaard, S. QUASES (QUantitative Analysis of Surfaces by Electron Spectroscopy) http://www.quases.com/home/ (accessed 2021 -02 -14).
(38) Tanuma, S.; Powell, C. J.; Penn, D. R. Calculations of Electron Inelastic Mean Free Paths. V. Data for 14 Organic Compounds over the 50–2000 EV Range. *Surf. Interface Anal.* **1994**, *21* (3), 165–176. https://doi.org/10.1002/sia.740210302.
(39) Gullikson, E. M. CXRO X-Ray Interactions With Matter http://henke.lbl.gov/optical_constants/ (accessed 2021 -02 -14).
(40) Blum, M.; Odelius, M.; Weinhardt, L.; Pookpanratana, S.; Bär, M.; Zhang, Y.; Fuchs, O.; Yang, W.; Umbach, E.; Heske, C. Ultrafast Proton Dynamics in Aqueous Amino Acid Solutions Studied by Resonant Inelastic Soft X-Ray Scattering. *J. Phys. Chem. B* **2012**, *116* (46), 13757–13764. https://doi.org/10.1021/jp302958j.

(41) Heske, C.; Zharnikov, M.; Weinhardt, L.; Blum, M.; Weigand, M.; Zubavichus, Y.; Bar, M.; Maier, F.; Denlinger, J. D.; Fuchs, O.; Grunze, M.; Umbach, E. Reply to Comment on "Isotope and Temperature Effects in Liquid Water Probed by X-Ray Absorption and Resonant X-Ray Emission Spectroscopy." *Phys. Rev. Lett.* **2008**, *100*.

(42) Weinhardt, L.; Fuchs, O.; Fleszar, A.; Bär, M.; Blum, M.; Weigand, M.; Denlinger, J. D.; Yang, W.; Hanke, W.; Umbach, E.; Heske, C. Resonant Inelastic Soft X-Ray Scattering of CdS: A Two-Dimensional Electronic Structure Map Approach. *Phys. Rev. B* **2009**, *79* (16), 165305. https://doi.org/10.1103/PhysRevB.79.165305.

(43) Meyer, F.; Blum, M.; Benkert, A.; Hauschild, D.; Nagarajan, S.; Wilks, R. G.; Andersson, J.; Yang, W.; Zharnikov, M.; Bär, M.; Heske, C.; Reinert, F.; Weinhardt, L. "Building Block Picture" of the Electronic Structure of Aqueous Cysteine Derived from Resonant Inelastic Soft X-Ray Scattering. *J. Phys. Chem. B* **2014**, *118* (46), 13142–13150. https://doi.org/10.1021/jp5089417.

(44) Meyer, F.; Blum, M.; Benkert, A.; Hauschild, D.; Jeyachandran, Y. L.; Wilks, R. G.; Yang, W.; Bär, M.; Heske, C.; Reinert, F.; Zharnikov, M.; Weinhardt, L. X-Ray Emission Spectroscopy of Proteinogenic Amino Acids at All Relevant Absorption Edges. *J. Phys. Chem. B* **2017**, *121* (27), 6549–6556. https://doi.org/10.1021/acs.jpcb.7b04291.

(45) Weinhardt, L.; Benkert, A.; Meyer, F.; Blum, M.; Hauschild, D.; Wilks, R. G.; Bär, M.; Yang, W.; Zharnikov, M.; Reinert, F.; Heske, C. Local Electronic Structure of the Peptide Bond Probed by Resonant Inelastic Soft X-Ray Scattering. *Phys. Chem. Chem. Phys.* **2019**. https://doi.org/10.1039/C9CP02481F.

(46) Stöhr, J. *NEXAFS Spectroscopy*; Springer Series in Surface Sciences; Springer-Verlag: Berlin Heidelberg, 1992. https://doi.org/10.1007/978-3-662-02853-7.

(47) Zubavichus, Y.; Shaporenko, A.; Korolkov, V.; Grunze, M.; Zharnikov, M. X-Ray Absorption Spectroscopy of the Nucleotide Bases at the Carbon, Nitrogen, and Oxygen K-Edges. *J. Phys. Chem. B* **2008**, *112* (44), 13711–13716. https://doi.org/10.1021/jp802453u.

(48) Plekan, O.; Feyer, V.; Richter, R.; Coreno, M.; de Simone, M.; Prince, K. C.; Carravetta, V. An X-Ray Absorption Study of Glycine, Methionine and Proline. *J. Electron Spectrosc. Relat. Phenom.* **2007**, *155* (1), 47–53. https://doi.org/10.1016/j.elspec.2006.11.004.

(49) Meyer, F.; Weinhardt, L.; Blum, M.; Bär, M.; Wilks, R. G.; Yang, W.; Heske, C.; Reinert, F. Non-Equivalent Carbon Atoms in the Resonant Inelastic Soft X-Ray Scattering Map of Cysteine. *J. Chem. Phys.* **2013**, *138* (3), 034306. https://doi.org/10.1063/1.4774059.

(50) Ågren, H.; Luo, Y.; Gelmukhanov, F.; Jensen, H. J. Aa. Screening in Resonant X-Ray Emission of Molecules. *J. Electron Spectrosc. Relat. Phenom.* **1996**, *82* (1), 125–134. https://doi.org/10.1016/S0368-2048(96)03041-1.

(51) Fuchs, O.; Zharnikov, M.; Weinhardt, L.; Blum, M.; Weigand, M.; Zubavichus, Y.; Bär, M.; Maier, F.; Denlinger, J. D.; Heske, C.; Grunze, M.; Umbach, E. Isotope and Temperature Effects in Liquid Water Probed by X-Ray Absorption and Resonant X-Ray Emission Spectroscopy. *Phys. Rev. Lett.* **2008**, *100* (2), 027801. https://doi.org/10.1103/PhysRevLett.100.027801.

(52) Weinhardt, L.; Weigand, M.; Fuchs, O.; Bär, M.; Blum, M.; Denlinger, J. D.; Yang, W.; Umbach, E.; Heske, C. Nuclear Dynamics in the Core-Excited State of Aqueous Ammonia Probed by Resonant Inelastic Soft x-Ray Scattering. *Phys. Rev. B* **2011**, *84* (10), 104202. https://doi.org/10.1103/PhysRevB.84.104202.

(53) Weinhardt, L.; Ertan, E.; Iannuzzi, M.; Weigand, M.; Fuchs, O.; Bär, M.; Blum, M.; Denlinger, J. D.; Yang, W.; Umbach, E.; Odelius, M.; Heske, C. Probing Hydrogen Bonding Orbitals: Resonant Inelastic Soft X-Ray Scattering of Aqueous NH_3. *Phys. Chem. Chem. Phys.* **2015**, *17* (40), 27145–27153. https://doi.org/10.1039/C5CP04898B.

(54) Jeyachandran, Y. L.; Meyer, F.; Nagarajan, S.; Benkert, A.; Bär, M.; Blum, M.; Yang, W.; Reinert, F.; Heske, C.; Weinhardt, L.; Zharnikov, M. Ion-Solvation-Induced Molecular Reorganization in Liquid

Water Probed by Resonant Inelastic Soft X-Ray Scattering. *J. Phys. Chem. Lett.* **2014**, *5* (23), 4143–4148. https://doi.org/10.1021/jz502186a.

(55) Jeyachandran, Y. L.; Meyer, F.; Benkert, A.; Bär, M.; Blum, M.; Yang, W.; Reinert, F.; Heske, C.; Weinhardt, L.; Zharnikov, M. Investigation of the Ionic Hydration in Aqueous Salt Solutions by Soft X-Ray Emission Spectroscopy. *J. Phys. Chem. B* **2016**, *120* (31), 7687–7695. https://doi.org/10.1021/acs.jpcb.6b03952.

TOC-Image:

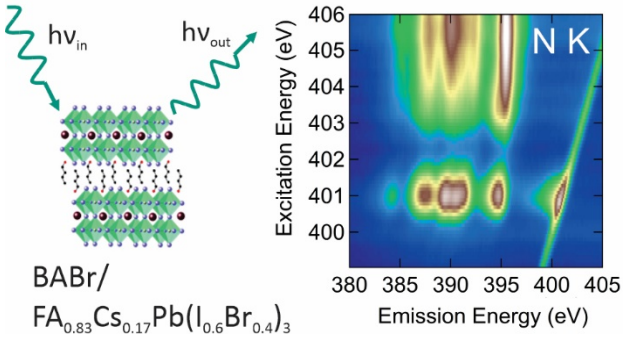
hν in
hν out
BABr/
FA0.83Cs0.17Pb(I0.6Br0.4)3
406
405
404
403
402
401
400
Excitation Energy (eV)
N K
380 385 390 395 400 405
Emission Energy (eV)